Diverse structures and emission properties of Copper(I) iodide complexes based on oxadiazole-type ligand

Alexey Gusev,[a*] Mikhail Kiskin,[b] Elena Braga,[a] Ekaterina Zamnius,[a] Konstantin Zakharov,[a] Andrey Tyutyunik,[a] Valery G. Vlasenko,[c] Ekaterina Zueva,[d] Maria Petrova,[d] and Wolfgang Linert[e]

[a.] *V.I. Vernadsky Crimean federal university, Simferopol, 295007, Crimea.*
[b.] *N.S. Kurnakov Institute of General and Inorganic Chemistry, Russian Academy of Sciences, Moscow, 119991, Russia.*
[c.] *Institute of Physics, Southern Federal University, 344090 Rostov-on-Don, Russia*
[d.] *Department of Inorganic Chemistry, Kazan National Research Technological University, Karl Marx Street 68, Kazan 420015, Russia.*
[e.] *Institute of Applied Physics, Vienna University of Technology, Wiedner Hauptstraße 8-10, 1040 Vienna, Austria, Austria.*

Table S1. Crystal data and structure refinements for complexes **1**–**4**.

Compound/Parameter	**1**·2$CHCl_3$	**2**	**3**	**4**
Chemical formula	$C_{62}H_{48}Cu_2I_2N_6O_2P_2$·2($CHCl_3$)	$C_{49}H_{40}CuIN_3OP_2$·CH_4O	$C_{26}H_{18}CuIN_6O_2$·C_2H_3N	$C_{13}H_9CuIN_3O$
M_r	1590.62	971.26	677.96	413.67
Crystal system, space group	Triclinic, $P\bar{1}$	Monoclinic, $P2_1/c$	Monoclinic, $C2/c$	Monoclinic, $P2_1/c$
Temperature (K)	100	100	150	150
a (Å) b (Å) c (Å)	9.2193(5) 13.6159(8) 13.7054(8)	9.8465(7) 13.3286(11) 33.4218(16)	31.569(7) 12.141(3) 14.223(3)	11.0011(13) 8.2803(9) 14.8098(16)
α (°) β (°) γ (°)	88.222(2) 78.591(2) 74.893(2)	93.900(2)	103.726(5)	104.035(2)
V (Å^3)	1627.77(16)	4376.1(5)	5296(2)	1308.8(3)
Z	1	4	8	4
Radiation type	Mo $K\alpha$	Mo $K\alpha$	Mo $K\alpha$	Mo $K\alpha$
m (mm^{-1})	1.945	1.321	2.031	4.021
d_{calc} (g·cm^{-3})	1.623	1.474	1.701	2.099
Crystal size (mm)	0.21 × 0.12 × 0.04	0.24 × 0.11 × 0.08	0.18 × 0.16 × 0.02	0.18 × 0.16 × 0.1
T_{min}, T_{max}	0.575, 0.746	0.586, 0.747	0.634, 0.746	0.611, 0.746
No. of measured, independent and observed [$I > 2\sigma(I)$] reflections	30800, 9927, 7780	32504, 10276, 7719	11755, 6304, 3905	8063, 3230, 3085
R_{int}	0.048	0.061	0.058	0.027
(sin θ)/λ_{max} (Å^{-1})	0.714	0.658	0.705	0.709
$R[F^2 > 2\sigma(F^2)]$, $wR(F^2)$, S	0.041, 0.081, 1.03	0.046, 0.114, 1.03	0.051, 0.142, 0.99	0.020, 0.050, 1.06
No. of reflections	9927	10276	6304	3230
No. of parameters	389	534	353	172
H-atom treatment	H-atom parameters constrained	H-atom parameters constrained	H-atom parameters constrained	H-atom parameters constrained
$\Delta\rho_{max}$, $\Delta\rho_{min}$ (e Å^{-3})	1.33, -1.11	1.19, -0.69	0.87, -1.48	0.42, -0.45

Table S2. Selected bond lengths and angles of complexes **1**–**4**.

1·2$CHCl_3$	**2**	**3**	**4**
Bond length (Å)			
I1-Cu1 2.6579(4)	I1-Cu1 2.6730(6)	I1-Cu1 2.6093(9)	I1-Cu1 2.5941 (4)
Cu1-P1 2.2356(8)	Cu1-P2 2.2707(11)	Cu1-N1 2.064(5)	I1-Cu1i 2.6147 (3)
I1-Cu1i 2.6909(4)	Cu1-P1 2.2707(10)	I1-Cu1i 2.6857(10)	Cu1-Cu1i 2.8579 (5)
Cu1-N1 2.052(2)	Cu1-N1 2.115(3)	Cu1-N4 2.068(5)	Cu1-N1 2.0653 (16)
Cu1-Cu1i 2.9863(7)		Cu1-Cu1i 2.6810(15)	Cu1-N2ii 2.0861 (16)
Angles (deg.)			
I1-Cu1-I1i 112.126(13)	P1-Cu1-I1 113.91(3)	I1-Cu1-I1i 119.18(3)	I1-Cu1-I1i 113.448 (10)
P1-Cu1-Cu1i 126.56(3)	N1-Cu1-I1 103.47(9)	N1-Cu1-Cu1i 123.17(14)	I1-Cu1-Cu1i 57.070 (9)
I1-Cu1-Cu1i 56.589(12)	P1-Cu1-P2 127.29(4)	I1-Cu1-Cu1i 61.00(3)	I1i-Cu1-Cu1i 56.378 (11)
N1-Cu1-I1i 104.58(7)	N1-Cu1-P1 104.03(9)	N1-Cu1-N4 111.42(19)	N1-Cu1-I1 107.63 (5)
I1i-Cu1-Cu1i 55.537(12)	P2-Cu1-I1 103.59(3)	Cu1i-Cu1-I1i 58.18(3)	N1-Cu1-I1i 110.28 (5)
N1-Cu1-I1 104.12(7)	N1-Cu1-P2 101.54(9)	N4-Cu1-I1i 104.19(14)	N1-Cu1-Cu1i 126.30 (4)
P1-Cu1-I1 108.20(2)		N1-Cu1-I1 110.08(13)	N1-Cu1-N2ii 98.27 (6)
N1-Cu1-Cu1i 116.36(7)		N4-Cu1-I1 109.42(13)	N2ii-Cu1-I1 119.50 (5)
P1-Cu1-I1i 110.64(2)		N1-Cu1-I1i 102.28(14)	N2ii-Cu1-I1i 106.54 (5)
N1-Cu1-P1 117.07(7)		N4-Cu1-Cu1i 124.68(14)	N2ii-Cu1-Cu1i 135.03 (4)

Table S3. Selected parameters of π…π intermolecular interactions in **1**·2$CHCl_3$, **2**, **3**, and **4** (C_g…C_g = distance between ring centroids (Å); α = dihedral angle between planes I and J (deg.); C_g(I)_Perp = perpendicular distance of C_g(I) on ring J (Å); Slippage = distance between C_g(I) and perpendicular projection of C_g(J) on ring I (Ang) (Å); the analysis was done using PLATON software [A. L. Spek, Acta Cryst. 2009, D65, 148-155]).

Contact C_g…C_g	Symmetry index	C_g…C_g, Å	α, deg.	C_g(I)_Perp, Å	Slippage, Å
1·2$CHCl_3$					
C_{g3}(N1C1-C5)…C_{g4}(C8-C13)	1-X, 2-Y, 1-Z	3.7735(17)	4.91(13)	3.3189(11)	1.508
2					
C_{g1}(O1C6N3N2C7)…C_{g3}(C8-C13)	-X, -Y, 1-Z	3.677(2)	3.2(2)	3.2547(17)	1.772
C_{g1}(O1C6N3N2C7)…C_{g9}(C44-C49)	1-X, 1-Y, 1-Z	3.825(2)	12.3(2)	3.3462(17)	1.614
3					
C_{g2}(O1C6N2N3C7)…C_{g6}(C8-C13)	-X, Y, 3/2-Z	3.516(3)	7.2(3)	3.438(2)	1.160
C_{g3}(O2C19N5N6C20)…C_{g3}	1-X, Y, 3/2-Z	3.889(3)	1.8(3)	3.520(2)	1.655
C_{g3}(O2C19N5N6C20)…C_{g7}(C11-C26)	1-X, 1-Y, 2-Z	3.539(3)	2.5(3)	3.331(2)	1.318
C_{g4}(N1C1-C5)…C_{g6}(C8-C13)	-X, 1-Y, 1-Z	3.891(4)	9.7(3)	3.374(2)	1.711
C_{g5}(N4C14-C18)…C_{g7}(C11-C26)	1-X, Y, 3/2-Z	3.850(4)	9.1(3)	3.463(2)	1.700
4					
C_{g2}(N1C1-C5)…C_{g4}(C8-C13)	2-X, 1-Y, 1-Z	3.7535(12)	0.88(10)	3.2577(7)	1.861

Table S4. Intra- and intermolecular Y-X…π interactions in the crystal packing of **1**·2$CHCl_3$ and **2** (C_g(J) is a centroid of benzoic ring J; X…C_g is a distance of X to C_g; X-Perp is a perpendicular distance of H to ring plane J; γ is an angle between C_g-H vector and ring J normal; Y-X...C_g is X-H-C_g angle).

Contact Y-X...C_g	Symmetry index	X...C_g, Å	γ, deg.	Y-X...C_g, deg.	Y..C_g, Å
1·2$CHCl_3$					
C10-H10…C_{g6}(C20-C25)	1-X, 2-Y, 1-Z	2.70	8.49	158	3.596(3)
C16-H16…C_{g3}(N1C1-C5)	-X, 1-Y, 1-Z	2.92	8.95	125	3.553(3)
C23-H23…C_{g7}(C26-C31)	1+X, Y ,Z	2.76	11.60	148	3.599(4)
C30-H30…C_{g5}(C14-C19)	-X, 1-Y, -Z	2.97	9.91	137	3.717(3)
C32-Cl1…C_{g2}(O1C6N2N3C7)	X, Y, -1+Z	3.5331(19)	6.09	130.89(15)	4.858(4)
C32-Cl2…C_{g6}(C20-C25)	1-X, 1-Y, -Z	3.9284(19)	21.85	157.33(15)	5.578(4)
2					
C24-H24…C_{g7}(C32-C37)	1-X, -1/2+Y, 1/2-Z	2.83	11.25	143	3.633(4)
C25-H25…C_{g8}(C38-C43)	1-X, -1/2+Y, 1/2-Z	2.96	13.09	147	3.789(4)
C30-H30…C_{g5}(C20-C25)	1-X, -1/2+Y, 1/2-Z	2.92	9.96	142	3.710(5)
C33-H33…C_{g4}(C14-C19)	-	2.74	12.39	138	3.508(4)
C36-H36…C_{g3}(C8-C13)	-X, 1-Y, 1-Z	2.80	7.88	164	3.724(4)
C41-H41…C_{g4}(C14-C19)	1-X, 1/2+Y, 1/2-Z	2.79	10.99	134	3.518(5)
C48-H48…C_{g7}(C32-C37)	1-X, 1-Y, 1-Z	2.94	3.79	155	3.822(4)

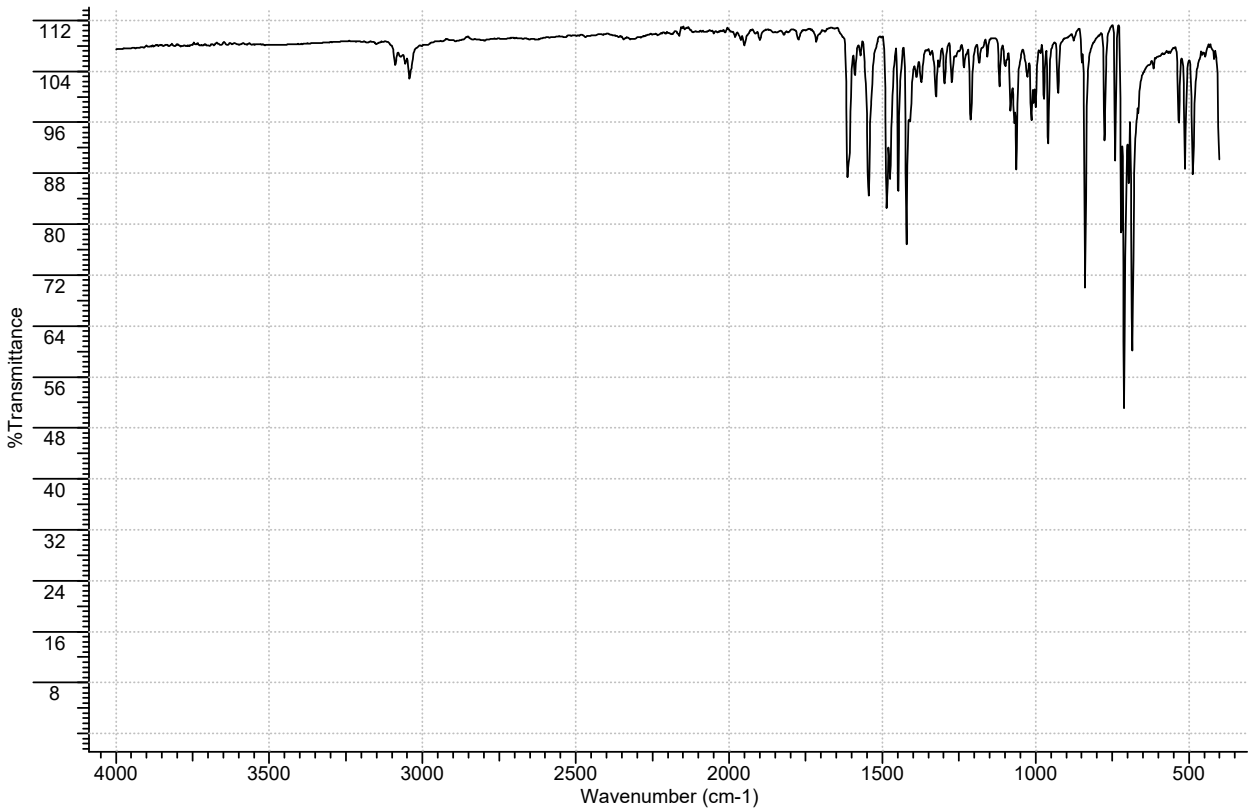

Figure S1. IR-spectrum of complex **1**.

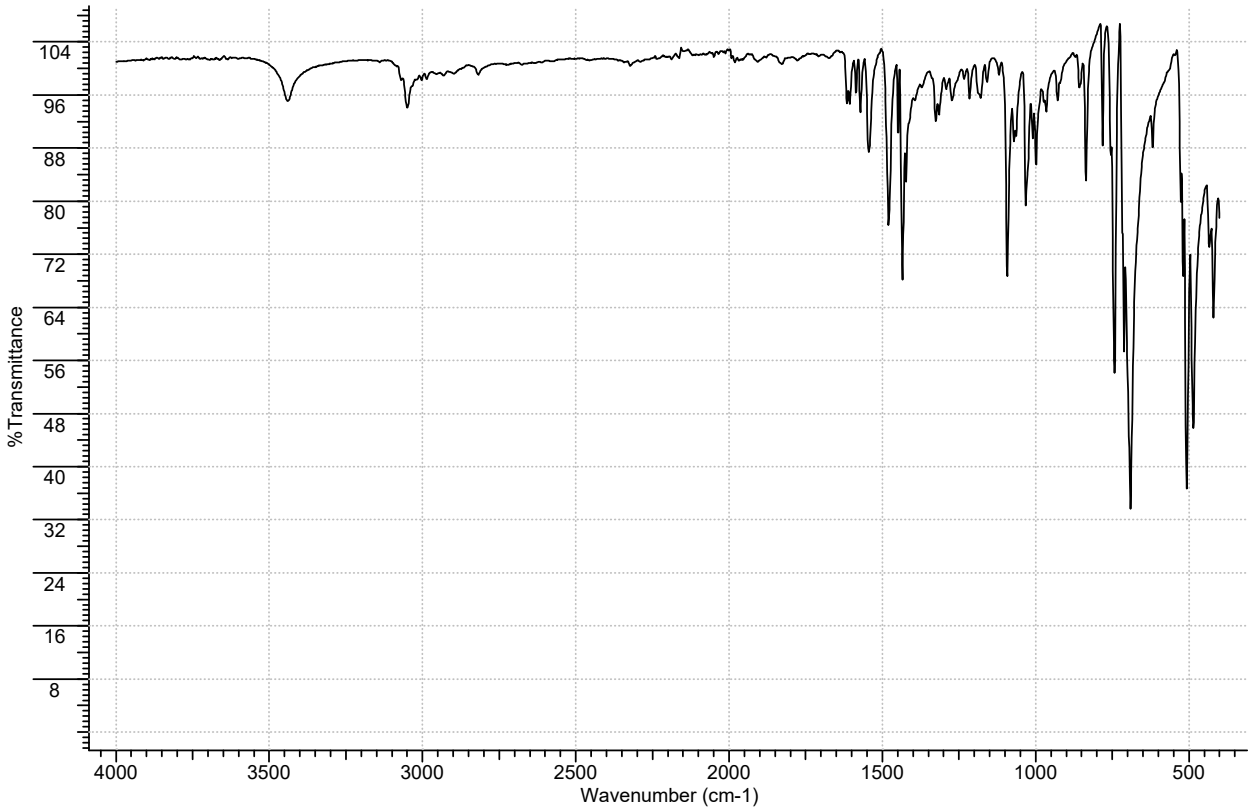

Figure S2. IR-spectrum of complex **2**.

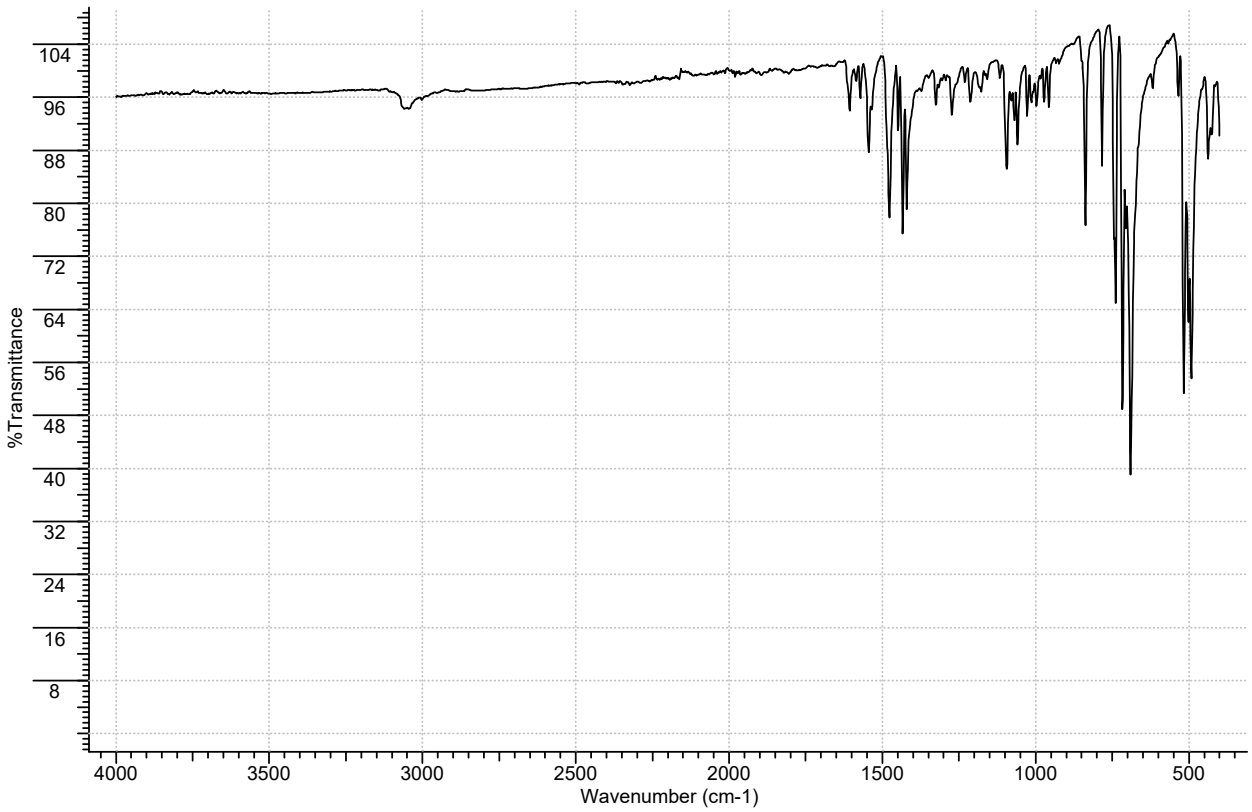

Figure S3. IR-spectra of complex **3**.

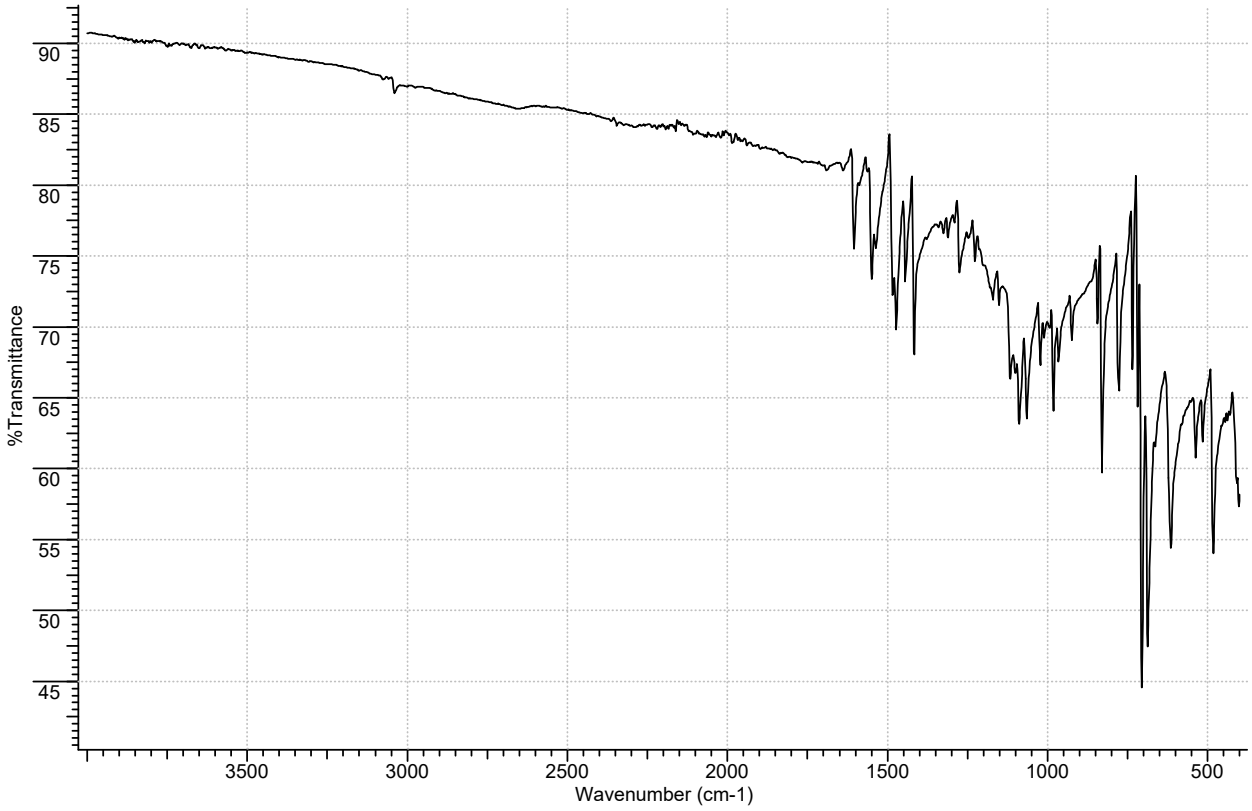

Figure S4. IR-spectra of complex **4**.

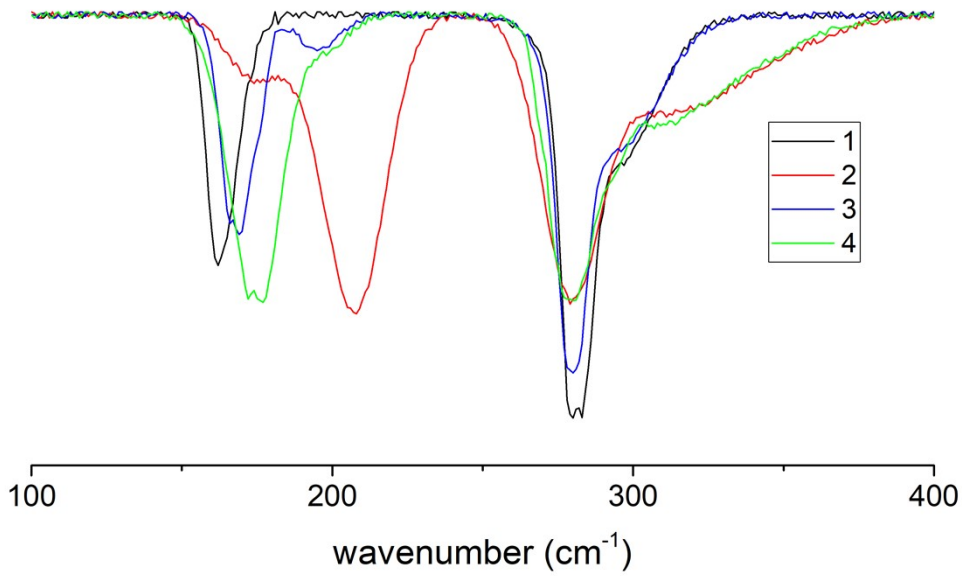

Figure S5. Far-IR-spectra of complexes **1**–**4**.

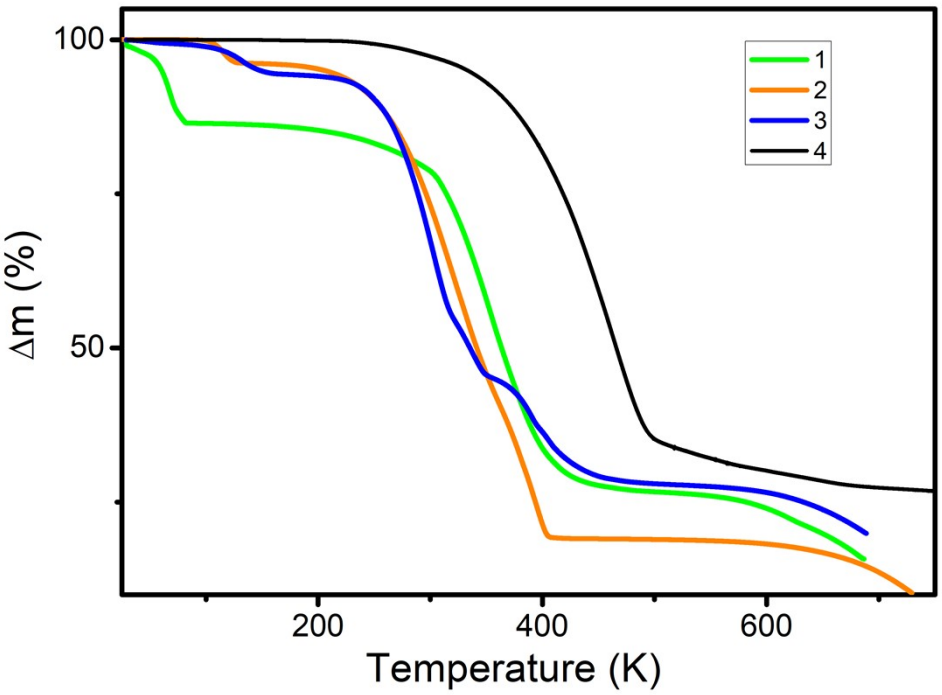

Figure S6. TGA curves of complexes **1**·2$CHCl_3$, **2**, **3**, and **4**.

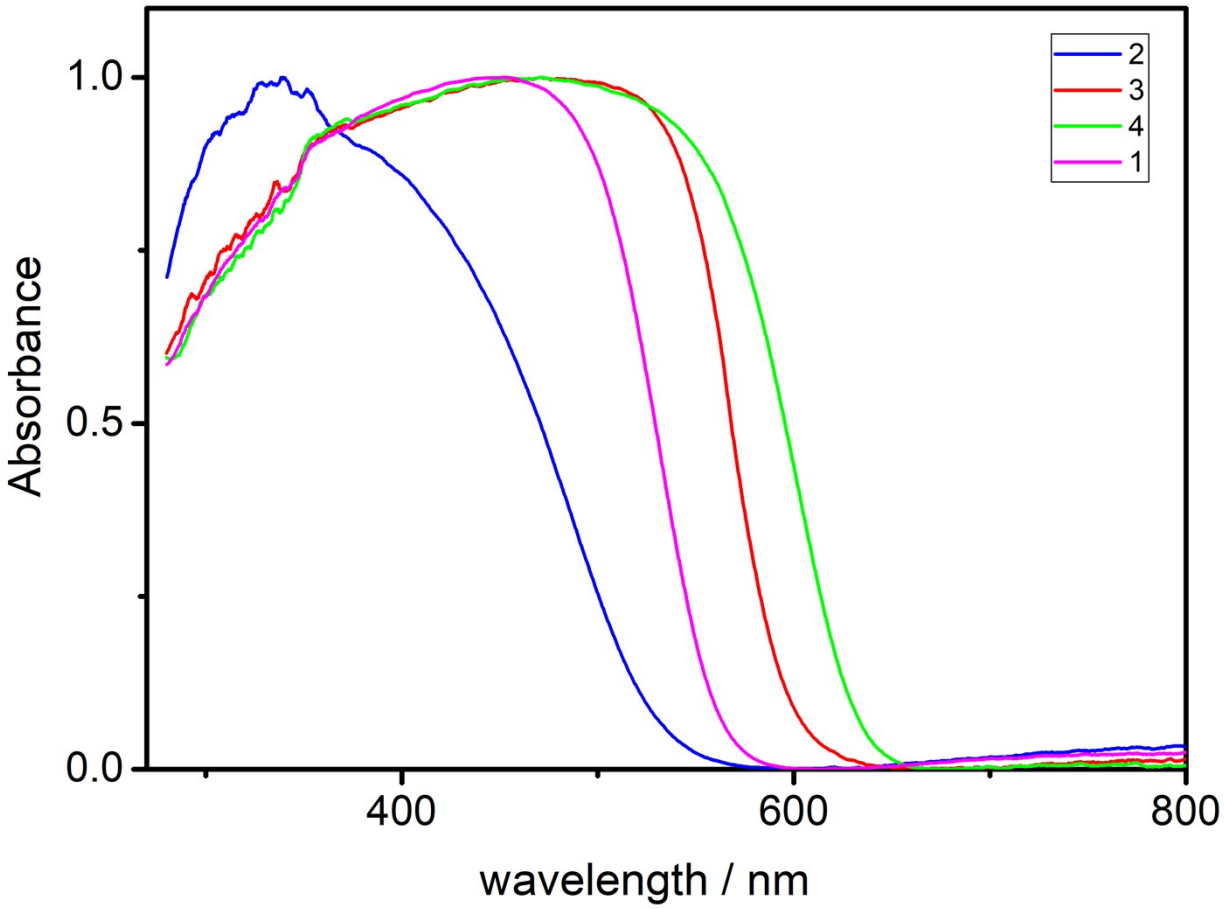

Figure S7. Normalized absorption spectra of **1**·2$CHCl_3$, **2**, **3**, and **4** in solid state.

Interpretation of electronic absorption spectra (EAS) of complexes 1 and 3 based on TDDFT calculations.

For complexes **1** and **3**, the characteristics of singlet-singlet electronic transitions were calculated and their assignments to the observed bands in the experimental solid-state EAS were performed. Figures S8 and S9 compares the experimental solid-state EAS with the calculated electronic transition data for complexes **1** and **3**. The theoretical EAS were constructed as a sum of Gaussian-type curves, where the position and amplitude were determined by the energies and oscillator strengths of the electronic transitions, respectively. The calculated energies (E), wavelengths of singlet-singlet transitions (λ_{cal}), oscillator strengths (f), along with the key frontier molecular orbitals (MOs) involved in these transitions, are summarized in Table 5. The energy level diagrams, isosurfaces of the frontier MOs, and wavelengths of calculated electronic transitions are presented in Figures S10 and S11.

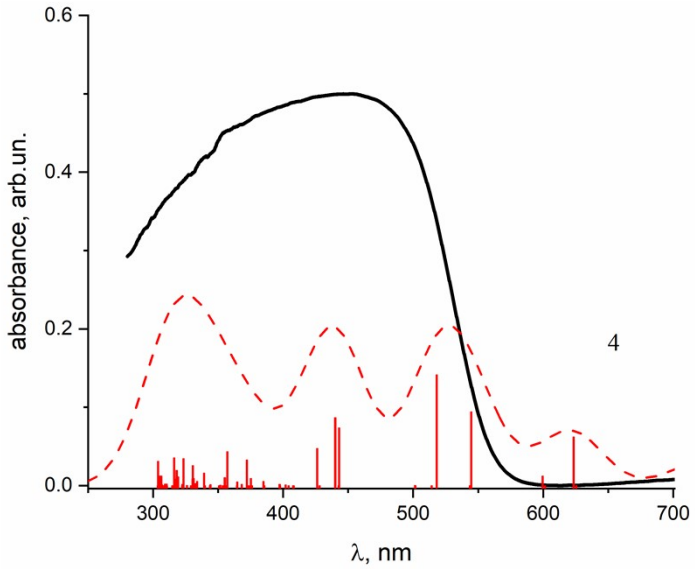

Figure S8. Experimental solid-state (solid black line) and theoretical (dashed red line) EAS of complex **1**. Vertical red lines mark the calculated absorption wavelengths (λ) scaled by their oscillator strengths (f).

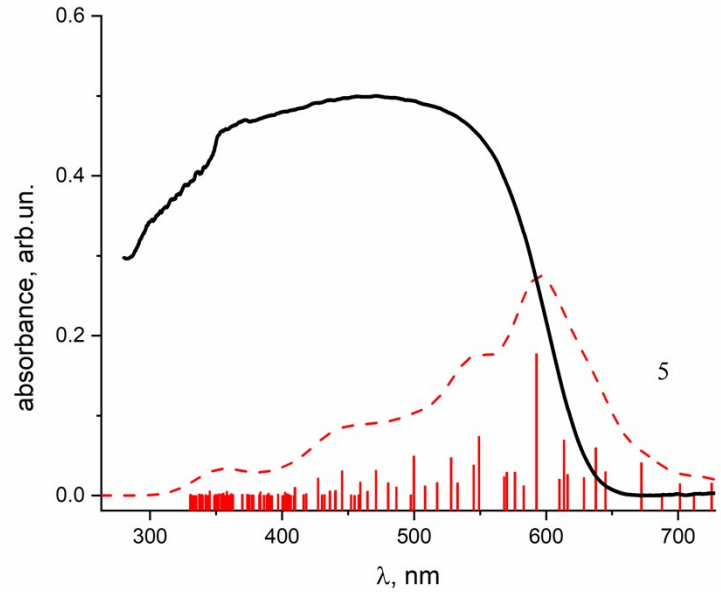

Figure S9. Experimental solid-state (solid black line) and theoretical (dashed red line) EAS of complex **2**. Vertical red lines mark the calculated absorption wavelengths (λ) scaled by their oscillator strengths (f).

Table S5. The wavelengths, energies, oscillator strengths, and the characters of vertical transitions to low-lying singlet excited states for complexes **1** and **3** (TDDFT data).

Comp.	State	λ, nm	E, eV	f	Excitations	Assignments
1	S_7	545	2.28	0.09	H–2 → L (79%)	d(Cu) → π*L (MLCT)
	S_9	518	2.39	0.14	H–4 → L (57%) H–3 → L+1 (16%)	d(Cu) → π*L (MLCT)
	S_{13}	443	2.80	0.07	H–6 → L (53%) H–7 → L+1 (24%)	d(Cu) → π*L (MLCT)
	S_{16}	440	2.82	0.09	H–6 → L (35%) H–7 → L+1 (31%) H → L+3 (12%) H–9 → L (12%)	d(Cu) → π*L (MLCT)
	S_{35}	357	3.47	0.04	H → L+10 (79%)	d(Cu) → π*TPP (MLCT) n(I) → π*TPP (XLCT)
3	S_{13}	638	1.94	0.06	H–2 → L+3 (67%)	d(Cu) → π*L (MLCT)
	S_{16}	614	2.02	0.07	H–3 → L+2 (23%) H–5 → L (22%) H–4 → L (15%)	d(Cu) → π*L (MLCT)
	S_{18}	593	2.09	0.18	H–3 → L+1 (27%) H–5 → L+1 (22%) H–3 → L+3 (13%)	d(Cu) → π*L (MLCT)
	S_{23}	549	2.26	0.07	H–6 → L (31%) H–6 → L+2 (25%) H–5 → L (15%) H–3 → L+2 (12%)	d(Cu) → π*L (MLCT)
	S_{26}	528	2.35	0.05	H–7 → L (30%) H–6 → L+2 (16%) H–7 → L+2 (12%)	d(Cu) → π*L (MLCT)
	S_{29}	500	2.48	0.05	H–8 → L (24%) H–7 → L+1 (20%) H–6 → L+3 (15%)	d(Cu) → π*L (MLCT)

In the solid state, both complexes **1** and **3** exhibit a broad absorption band spanning 300–600 nm, which, according to TDDFT calculations, arises from numerous singlet-singlet electronic transitions.

The calculated EAS of complex **1** is characterized by several singlet-singlet electronic transitions with oscillator strengths ranging from 0.04 to 0.14. The most intense transitions include S_7, S_9, S_{13}, S_{16}, and S_{35} states (Fig. S8 and S10).

(a) Transitions S_7 (545 nm, f = 0.09) and S_9 (518 nm, f = 0.14, the most intense transition) are characterized by the excitation H–2 [60%(Cu) + 32%(TPP) + 8%(L)] → L [98%(L) + 2%(Cu)] (79%) for S_7 and two excitations H–4 [62%(Cu) + 14%(TPP) + 20%(L) + 4%(I)] → L [98%(L) + 2%(Cu)] (57%) and H–3 → L+1 [94%(L) + 3%(Cu) + 3%(TPP)] (16%) for S_9. Both transitions involve the electron transfer from Cu(I) d-orbital to ligand π*-orbital and therefore exhibit the MLCT character.

(b) The S_{13} (443 nm, f = 0.07) and S_{16} (440 nm, f = 0.09) transitions are composed of two key excitations: H–6 [82%(Cu) + 10%(TPP) + 4%(L) + 4%(I)] → L [98%(L) + 2%(Cu)] (53%) and H–7 → L+1 [94%(L) + 3%(Cu) + 3%(TPP)] (24%) for S_{13} and H–6 [82%(Cu) + 10%(TPP) + 4%(L) + 4%(I)] → L [98%(L) + 2%(Cu)] (35%) and H–7 → L+1 [94%(L) + 3%(Cu) + 3%(TPP)] (31%) for S_{16}. These transitions also display the MLCT behavior with a minor contribution from iodine n-orbitals (XLCT), although the dominant mechanism remains the charge transfer from Cu(I) to ligand L.

(c) The S_{35} (357 nm, f = 0.04) transition is mainly (79%) composed of the excitation H [62%(Cu) + 18%(TPP) + 17%(I) + 3%(L)] → L+10 [93%(TPP) + 5%(Cu) + 2%(L)]. This transition exhibits a mixed character involving the charge transfer from Cu(I) d- and iodine n-orbitals to π*-orbital of TPP ligand (a combination of MLCT and XLCT).

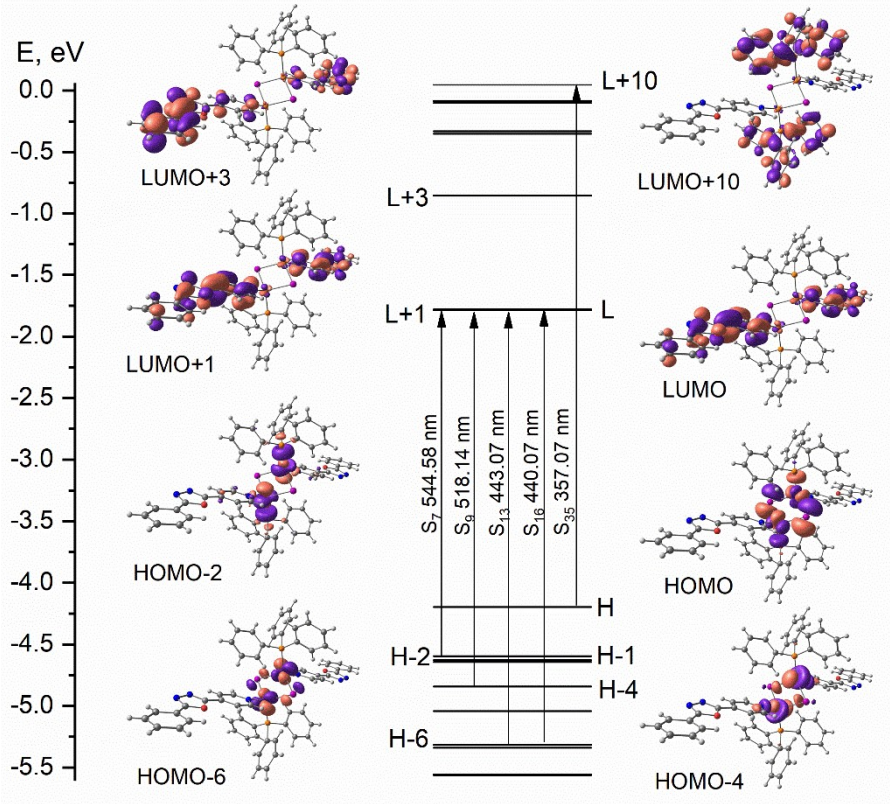

Figure S10. The energy level diagram, isosurfaces of the frontier MOs, and wavelengths of calculated electronic transitions for complex **1**.

The broad absorption band of complex **3** is attributed to a series of singlet-singlet electronic transitions with oscillator strengths in the range from 0.05 to 0.18. The most intense transitions include S_{13}, S_{16}, S_{18}, S_{23}, S_{26}, and S_{29} states (Fig. S9 and S11).

(a) Transition S_{13} (638 nm, f = 0.06) is characterized by the excitation H–2 [70%(Cu) + 7%(I) + 23%(L)] → L+3 [97%(L) + 3%(Cu)] (67%). Transition S_{16} (614 nm, f = 0.07) is composed of two key excitations: H–3 [67%(Cu) + 33%(L)] → L+2 [97%(L) + 3%(Cu)] (23%) and H–5 [71%(Cu) + 23%(L) + 5%(I)] → L [98%(L) + 2%(Cu)] (22%). Both transitions exhibit the MLCT character (involve the electron transfer from d-orbital of Cu(I) to π*-orbital of ligand L).

(b) Transition S_{18} (593 nm, f = 0.18, the most intense transition) has two main contributions: H–3 [67%(Cu) + 33%(L)] → L+1 [98%(L) + 2%(Cu)] (27%) and H–5 [71%(Cu) + 23%(L) + 5%(I)] → L+1 [98%(L) + 2%(Cu)] (22%). This transition also exhibits the MLCT character and plays a key role in shaping the absorption band due to its high oscillator strength.

(c) Transitions S_{23} (549 nm, f = 0.07) (involve H–6 [82%(Cu) + 18%(L)] → L [98%(L) + 2%(Cu)] (31%) and H–6 [82%(Cu) + 18%(L)] → L+2 [97%(L) + 3%(Cu)] (25%)), S_{26} (528 nm, f = 0.05) (involve H–7 [75%(Cu) + 25%(L)] → L [98%(L) + 2%(Cu)] (30%) and H–6 [82%(Cu) + 18%(L)] → L+2 [97%(L) + 3%(Cu)] (16%)) and S_{29} (500 nm, f = 0.05) (involve H–8 [69%(Cu) + 31%(L)] → L [98%(L) + 2%(Cu)] (24%) and H–7 [75%(Cu) + 25%(L)] → L+1 [98%(L) + 2%(Cu)] (20%)) display the MLCT character.

Based on the composition of the key frontier orbitals, it can be concluded that all these transitions share the same MLCT nature. Only in certain transitions (S_{16}, S_{18}) there is a minor contribution from iodine n-orbitals (XLCT), although it remains insignificant compared to the MLCT component.

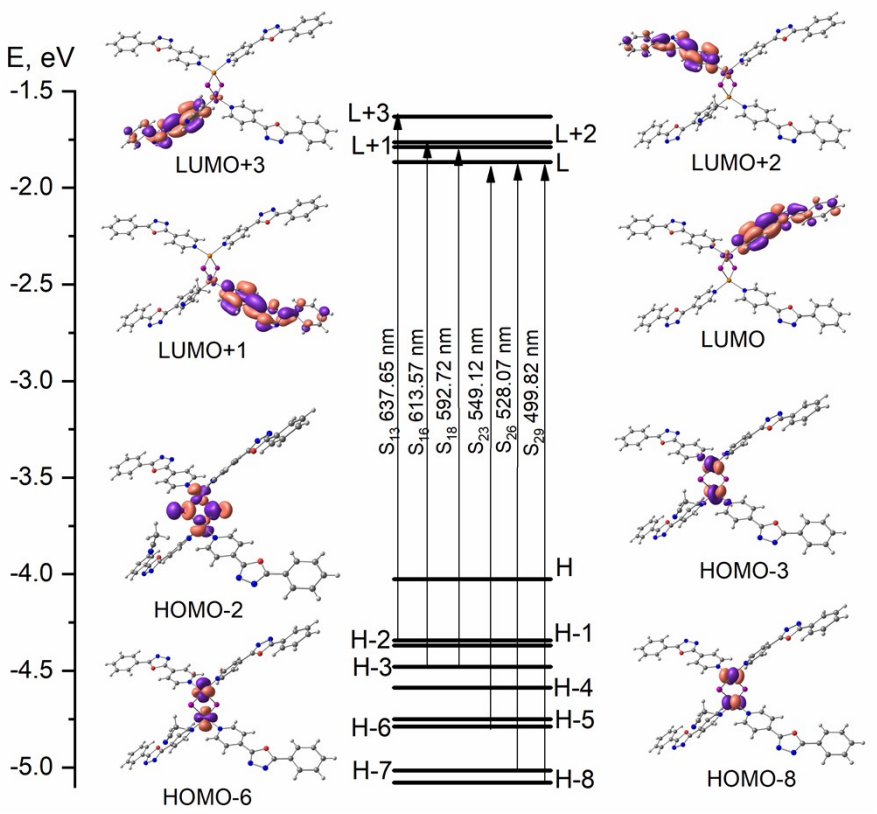

Figure S11. The energy level diagram, isosurfaces of the frontier MOs, and wavelengths of calculated electronic transitions for complex **2**.

Computational Details

All calculations were performed using Gaussian 09 [*M. J. Frisch, G. W. Trucks, H. B. Schlegel, G. E. Scuseria, M. A. Robb, J. R. Cheeseman, G. Scalmani, V. Barone, B. Mennucci, G. A. Petersson, H. Nakatsuji, M. Caricato, X. Li, H. P. Hratchian, A. F. Izmaylov, J. Bloino, G. Zheng, J. L. Sonnenberg, M. Hada, M. Ehara, K. Toyota, R. Fukuda, J. Hasegawa, M. Ishida, T. Nakajima, Y. Honda, O. Kitao, H. Nakai, T. Vreven, J. A. Montgomery, Jr., J. E. Peralta, F. Ogliaro, M. Bearpark, J. J. Heyd, E. Brothers, K. N. Kudin, V. N. Staroverov, R. Kobayashi, J. Normand, K. Raghavachari, A. Rendell, J. C. Burant, S. S. Iyengar, J. Tomasi, M. Cossi, N. Rega, J. M. Millam, M. Klene, J. E. Knox, J. B. Cross, V. Bakken, C. Adamo, J. Jaramillo, R. Gomperts, R. E. Stratmann, O. Yazyev, A. J. Austin, R. Cammi, C. Pomelli, J. W. Ochterski, R. L. Martin, K. Morokuma, V. G. Zakrzewski, G. A. Voth, P. Salvador, J. J. Dannenberg, S. Dapprich, A. D. Daniels, Ö. Farkas, J. B. Foresman, J. V. Ortiz, J. Cioslowski, and D. J. Fox, Gaussian, Inc., Wallingford CT, 2009*]. Excitation spectra were obtained using time-dependent density-functional theory (TDDFT) with Becke's one-parameter hybrid functional and Lee-Yang-Parr's gradient corrected correlation functional B1LYP (25% HF exchange) [*A.D. Becke. Density-functional thermochemistry. III. The role of exact exchange. J. Chem. Phys., 98 (7) (1993), pp. 5648-5652, C. Lee, W. Yang, R.G. Parr. Development of the Colle-Salvetti correlation-energy formula into a functional of the electron density. Phys. Rev. B, 37 (2) (1988), p. 785*]. LANL2DZ relativistic effective core potential (RECP) basis set for I atoms and 6-31G(d,p) basis set for all other atoms were used. The electron excitation analysis was done with Chemissian software (version 4.23) [*http://www.chemissian.com*].

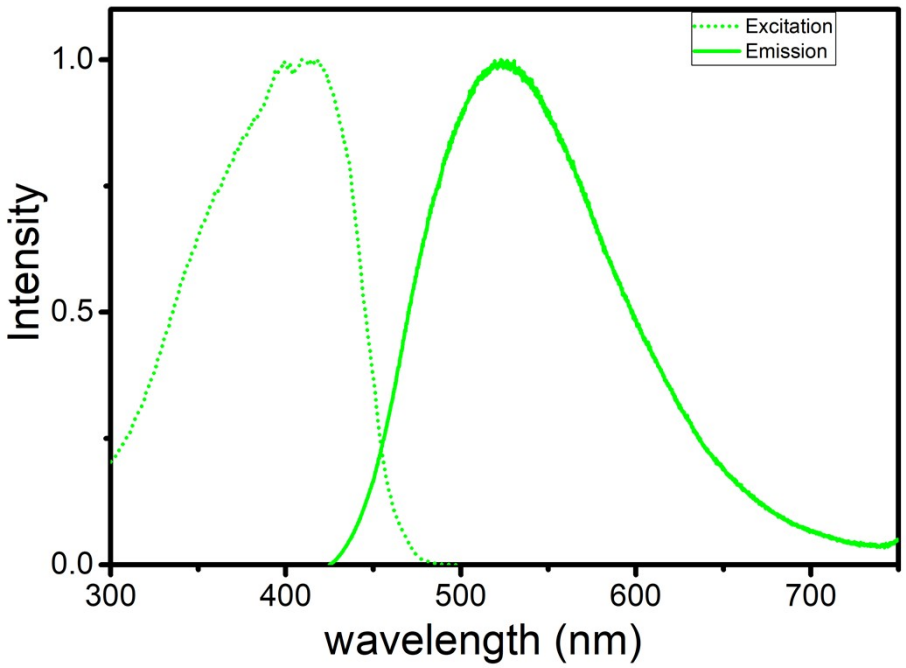

Figure S12. Excitation and emission spectra of solid **2** at 298 K (λ_{ex} = 395 nm).

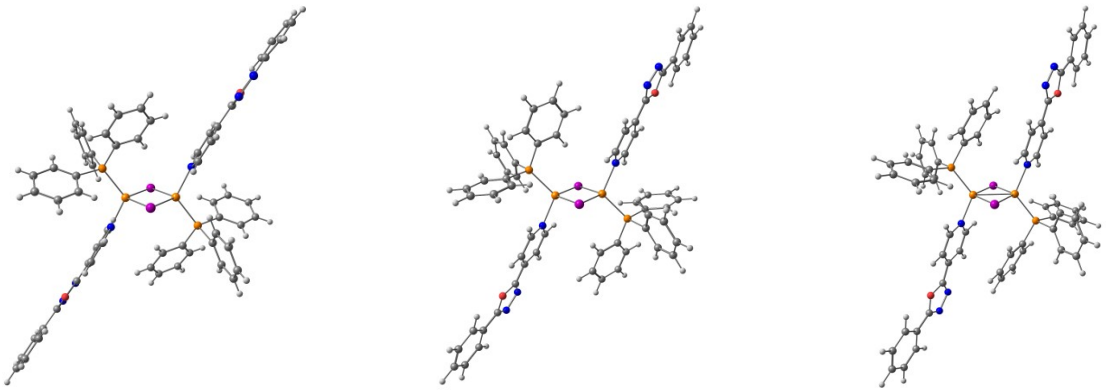

X-ray data PBE0/def2-TZVP PBE0-D3/def2-TZVP

Figure S13. DFT-optimized and crystallographically determined ground-state (S_0) geometries of complex **1**.

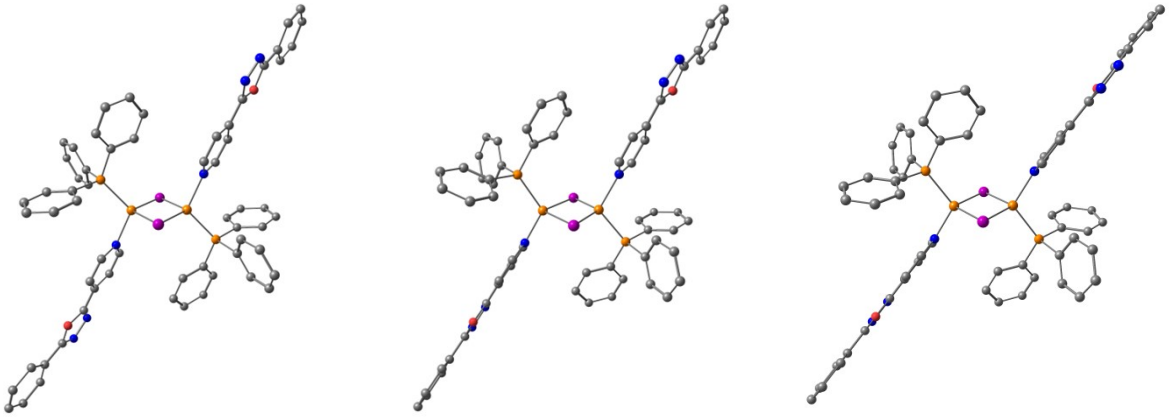

Figure S14. DFT-optimized ground/excited-state geometries of complex **1**.

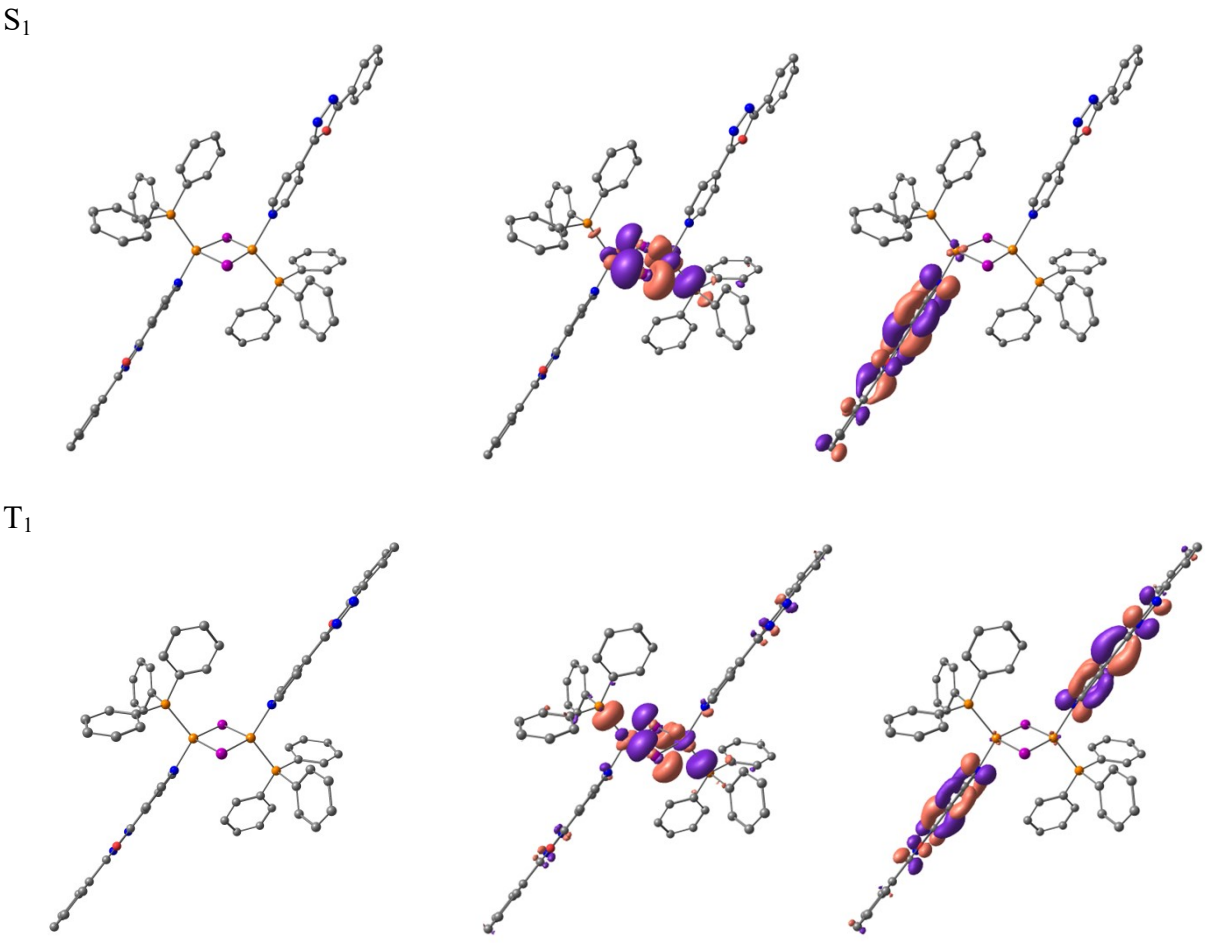

Figure S15. The equilibrium geometries and singly occupied molecular orbitals of complex **1** in the S_1 and T_1 excited states.

X-ray data PBE0/def2-TZVP

Figure S16. DFT-optimized and crystallographically determined ground-state (S_0) geometries of complex **2**.

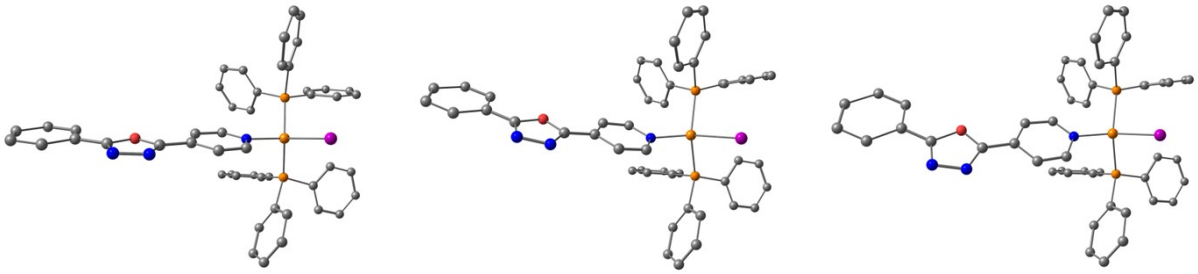

S_0 S_1 T_1

Figure S17. DFT-optimized ground/excited-state geometries of complex **2**.

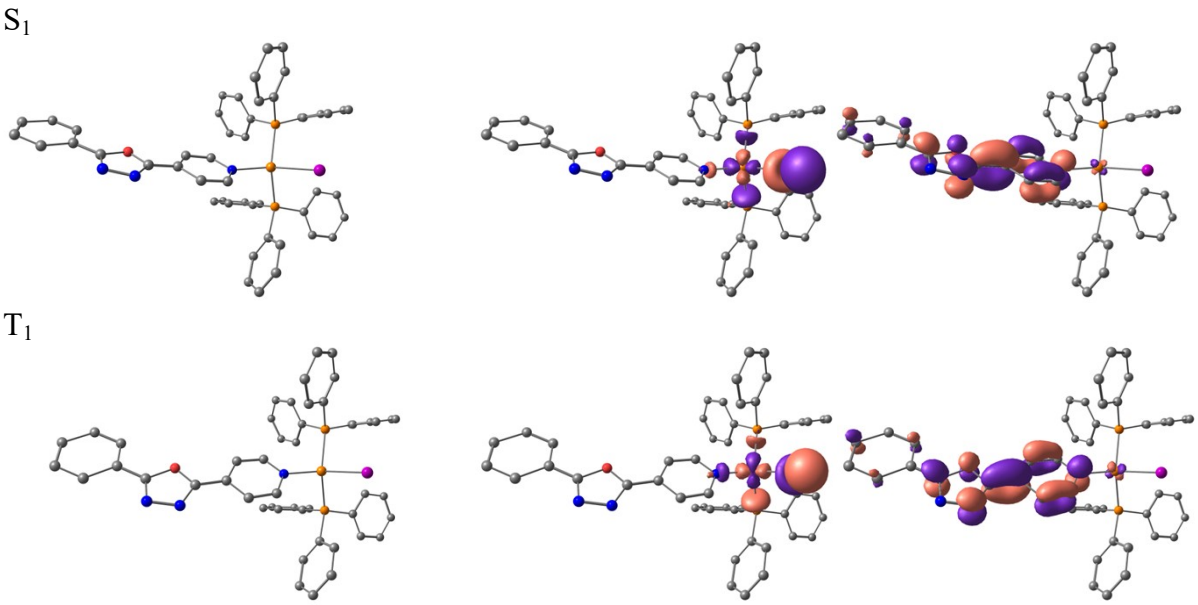

Figure S18. The equilibrium geometries and singly occupied molecular orbitals of complex **2** in the S_1 and T_1 excited states.